参赛学生姓名：Bai Theodore (白羽恩)

中学：北京一零一中学

省份：北京

国家/地区：中国

指导老师姓名：1、孙晓明；2、朱琳

指导老师单位：1、北京化工大学；2、北京一零一中学

论 文 题 目：Dual-Anion Electrolyte Engineering for Stable Seawater Oxidation

2026 S.-T. Yau High School Science Award
仅用于2026丘成桐中学科学奖论文公示

论文题目：**Dual-Anion Electrolyte Engineering for Stable Seawater Oxidation**

作者：**Bai Theodore** (白羽恩)

摘要：Alkaline seawater electrolysis represents a promising approach for large-scale green hydrogen production, leveraging abundant seawater feedstock. Nevertheless, its practical implementation faces severe challenges including chloride-induced corrosion, competitive parasitic oxidation, and transition-metal dissolution during the oxygen evolution reaction (OER). In this work, we propose a straightforward dual-anion electrolyte-engineering strategy by combining $F^-$ and $B(OH)_4^-$ to enhance seawater-oxidation stability. Benefiting from this dual-anion-assisted electrolyte, the FeNi-layered double hydroxide supported on nickel foam (FeNi-LDH/NF) maintains favorable OER activity and achieves stable operation for over 1500 h at 1 A $cm^{-2}$. By contrast, the blank electrode without anion additives fails after approximately 600 h. Comprehensive characterizations including XPS, operando Raman spectroscopy, metal-dissolution measurements, Bode impedance analysis, and molecular-dynamics simulations reveal the intrinsic synergy between $F^-$ and $B(OH)_4^-$. This synergistic effect suppresses near-surface $Cl^-$ accumulation and mitigates Ni/Fe dissolution. This work highlights that electrolyte engineering via $F^-$-$B(OH)_4^-$ dual-anion synergy serves as an effective strategy for constructing durable alkaline seawater-electrolysis systems.

关键词：NiFe-LDH; seawater electrolysis; oxygen evolution reaction; chloride corrosion; $F^-$+$B(OH)_4^-$ complex

2026 S.T.Yau High School Science Award
仅用于2026年丘成桐中学科学奖论文公示

目录:

1.Introduction.....4

2. Methodology.....6

2.1 Chemicals and materials.....6

2.2 Synthesis of NiFe-LDH.....6

2.3 Physical characterization.....6

2.4 Electrochemical Measurements.....6

2.5 In-situ electrochemical Raman measurements.....7

2.6 Molecular dynamic (MD) simulations.....7

3. Results and Discussion.....9

4. Conclusions.....18

5. References.....20

6. Acknowledgement.....23

2026 S.-T. Yau High School Science Award
仅用于2026丘成桐中学科学奖论文公示

论文正文：

## 1. Introduction

Hydrogen is expected to play a central role in future low-carbon energy systems [1–4]. Direct seawater electrolysis offers an appealing route to reduce freshwater consumption amid freshwater shortages [5–7]. Nevertheless, the complex composition of seawater brings harsher operating conditions, and chloride-induced anode degradation constitutes the major bottleneck for practical seawater electrolysis [8]. High-concentration $Cl^-$ readily accumulates at the electrode–electrolyte interface and penetrates porous catalyst layers, triggering corrosion and forming soluble metal-chloride species that accelerate transition-metal dissolution. Long-term alkaline seawater oxidation therefore requires coordinated regulation of chloride transport, metal dissolution and interfacial stability [9–13].

Substantial progress has been achieved in high-activity OER catalysts, yet long-term stability under practical conditions remains critical for alkaline seawater electrolysis [14–16]. Various stabilization strategies have been developed, including physical barrier coatings, dynamic surface reconstruction, doping, interlayer-anion engineering, electrolyte regulation and heterostructure engineering [17–22]. Anion-mediated protection has drawn growing interest, as surface oxyanions tailor the interfacial environment and restrict chloride access. In-situ generated sulfate from NiFe/$NiS_x$ and $Ni_3S_4$/NiFe-LDH, dynamically formed $WO_x$ from Nb-$WO_3$/$WS_2$, and released anions from CoFePBA/$Co_2P$ and CoFeAl-LDH can enrich at interfaces, repel $Cl^-$ and suppress degradation [16, 23–26] (as shown in Figure 1a). Exogenous electrolyte additives including sulfate, phosphate, $PF_6^-$ and $CrO_4^{2-}$ also stabilize LDH anodes via interfacial adsorption, excluding $Cl^-$ and mitigating metal dissolution [27–30]. Recent efforts further adopt complementary anion pairs such as $SO_4^{2-}$/$CO_3^{2-}$ and $MoO_4^{2-}$/$PO_4^{3-}$ for cooperative interfacial modulation and enhanced chloride rejection [31,32]. Fluoride, owing to its high electronegativity and strong hydration ability [33, 34], has been demonstrated to reorganize interfacial hydrogen-bond networks and regulate interfacial water structures (as shown in Figure 1b). Meanwhile, the hydroxyl-

2026 Siyau High School Science Award
仅用于2026年成利中学科学奖论文公示

rich structure and oxygen-coordination capability of borate favor its interaction with NiFe-based oxyhydroxides, enabling borate-mediated regulation of the local coordination environment and suppression of transition-metal dissolution during oxygen evolution [35-37].

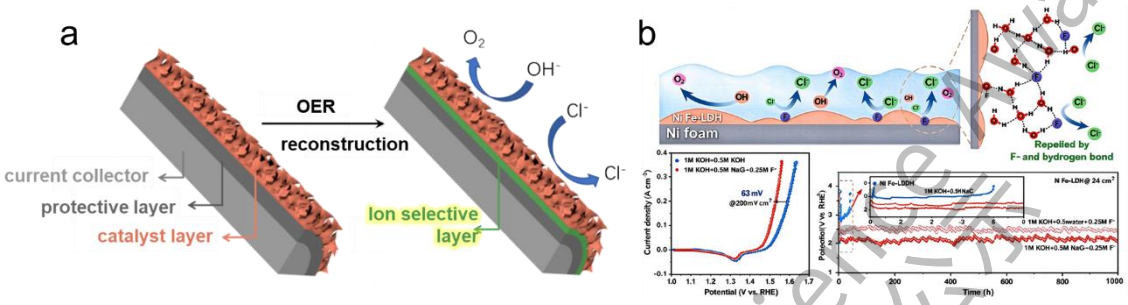
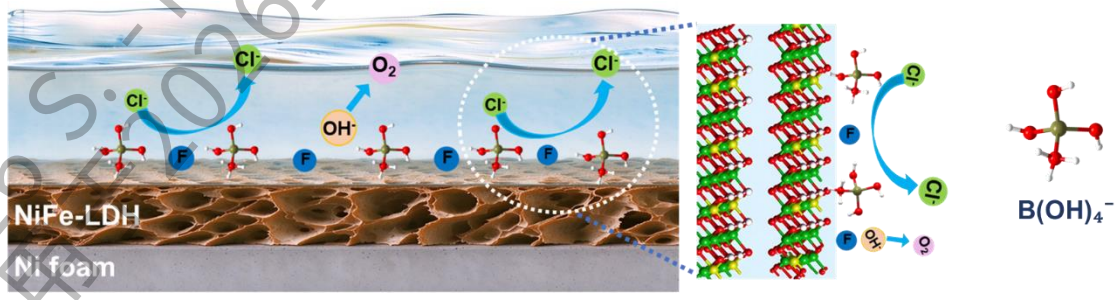



**Figure 1.** Classic approaches for electrode stabilization (a) Ion selective layer (ISL) [16], (b) $F^-$ electrolyte engineering [34]

Inspired by these merits, we developed an $F^-$+$B(OH)_4^-$ dual-anion coupled electrolyte engineering strategy to stabilize NiFe-LDH anodes for durable seawater oxidation. In detail, $F^-$ as a small ion with strong hydration ability can strongly interact with surrounding water molecules and $B(OH)_4^-$ contains several hydroxyl groups and can interact with water and NiFe-based oxyhydroxide surfaces. The introduced $F^-$ and $B(OH)_4^-$ not only repels $Cl^-$ to enhance corrosion resistance, but also suppresses transition-metal dissolution. As a result, FeNi-LDH/NF can stably electrolyze seawater for 1500 hours at 1 A $cm^{-2}$ in a $F^-$ and $B(OH)_4^-$-assisted electrolyte, significantly longer than in without additive electrolyte (600 h). This work highlights the impact of electrolyte regulation on the stability of electrocatalysis.




**Scheme 1.** Dual-anion coupled F-+B(OH)4- electrolyte engineering strategy

2026 S.-T. Yau High School Science Award
仅用于2026丘成桐中学科学奖公示

## 2. Methodology

### 2.1 Chemicals and materials:

$Ni(NO_3)_2 \cdot 6H_2O$ and $Fe(NO_3)_3 \cdot 9H_2O$ were purchased from Aladdin Industrial Co. Urea, KOH, and NaCl were purchased from Beijing Chemical Reagents Co. KF and $H_3BO_3$ were purchased from Shanghai Macklin Biochemical Co. Deionized water with a resistivity of ≥ 18 MΩ was utilized for preparation of all aqueous solutions. All reagents were of analytical grade and were employed directly without further purification. In strongly alkaline solutions, $H_3BO_3$ undergoes deprotonation, resulting in $B(OH)_4^-$ as the predominant borate species.

### 2.2 Synthesis of NiFe-LDH:

0.66 mmol $Ni(NO_3)_2 \cdot 6H_2O$, 0.33 mmol $Fe(NO_3)_3 \cdot 9H_2O$, and 5 mmol urea were dissolved in 35 mL deionized water. Nickel foam was subjected to ultrasonic cleaning in 3 M HCl for 5-10 minutes, followed by thorough rinsing with ethanol and deionized water. Subsequently, this solution and a piece of cleaned Ni foam measuring 2×4 $cm^2$ were transferred into a Teflon-lined stainless-steel autoclave and maintained at 120°C for 12 hours to synthesize the NiFe LDHs electrode.

### 2.3 Physical characterization:

XRD patterns were recorded on an Ultima IV (Rigaku) in the range from 5° to 90° at a scan rate of 5°/min. SEM images were obtained on a Zeiss SUPRA55 scanning electron microscope, operated at 10 kV. XPS was performed by using a K-Alpha model (Thermo Scientific). ICP-OES was carried out on the Thermo Fisher iCAP 7400.

### 2.4 Electrochemical Measurements:

A three-electrode system was employed to conduct all electrochemical measurements at a temperature of 25 °C. The electrocatalyst, with a working electrode surface area of 1 cm ×1 cm, utilized a Hg/HgO reference electrode and a graphite rod as the counter electrode. The measured potential versus Hg/HgO could be converted to the potential versus reversible hydrogen electrode (RHE) by Equation (1):

$$E_{\mathrm{RHE}} = E_{Hg/HgO} + 0.098 + 0.059 \times pH \quad (1)$$

OER performance was evaluated in alkaline simulated seawater with (1 M KOH



2026 S.-T. Yau High School Science Award 仅用于2026丘成桐中学科学奖论文公示

+ 0.5 M NaCl )_or without added halide ions (1 M KOH + 0.5 M NaCl + $X^-$). The electrochemical behavior was investigated using reverse linear sweep voltammetry (LSV) from 1 to 0 V vs Hg/HgO at a scan rate of 5 mV $s^{-1}$. The curves were manually corrected with 90% iR compensation. The R is obtained from electrochemical impedance spectroscopy (EIS), with the frequency range of $10^5$ to $10^{-1}$ Hz and an amplitude of 10 mV. Tafel slopes were derived by plotting potential against log(j) from the LSV curves.

The corrosion behavior was evaluated across various electrolytes using a conventional three-electrode system on an electrochemical workstation (CS2350H, Wuhan Corrtest Instruments). A piece of Ni foam (NF) with an exposed area of 1 × 1 $cm^2$ served as the working electrode, a platinum wire as the counter electrode, and a mercury/mercury oxide (Hg/HgO) electrode as the reference. The system could stabilize at the open-circuit potential until the potential drift was less than 1 mV/min. Polarization curves were then recorded from -0.3 V to 0.5 V versus the open-circuit potential at a scan rate of 0.5 mV $s^{-1}$ to determine the corrosion potential (Ecorr) and corrosion current density (icorr).

**2.5 In-situ electrochemical Raman measurements:**

Electrochemical Raman spectroscopy was carried out on a Horiba Lab RAM HR Evolution confocal Raman spectrometer equipped with a 532 nm laser source and a 50× objective lens, with an acquisition time of 90 seconds. The electrochemical workstation (CHI 660D, Chenhua, Shanghai) was used to perform the Amperometric i-t Test under OCP to 1.49V vs RHE. Each spectrum was obtained at least three times with an exposure time of 90 seconds.

**2.6 Molecular dynamic (MD) simulations:**

To simulate the distribution of OH- and Cl- on the electrode surface in various electrolytes, two models were constructed, representing simulated seawater and simulated seawater with an additional 1.5 M $F^-$, respectively, applied to the surface of a NiFe-LDH electrode model. Both electrolyte models contained 500 H2O molecules, 5 $Na^+$, 5 $Cl^-$, 10 $K^+$, and 10 $OH^-$ ions, while the $F^-$containing model additionally included

2026 S.-T. Yau High School Science Award
仅用于2026丘成桐中学科学奖论文公开

15 $K^+$ and 15 $F^-$ ions, and $F^-$+$B(OH)_4^-$ -containing model additionally included 4 $B(OH)_4^-$ and 6 $OH^-$. A vacuum layer approximately 30 Å was added above the solution to eliminate interactions between periodic images, resulting in a simulation box of approximately 36Å × 32Å × 60 Å. All atoms in the electrode model were fixed, while all particles in the solution could move freely. Periodic boundary conditions were applied along the x and y directions. Packmol was used to build the initial configurations of the model systems. The COMPASS III force field was used for molecular simulations. The Nosé–Hoover thermostat was applied to maintain constant NVT conditions with a relaxation time of 0.1 ps and a temperature of 300 K. The velocity Verlet algorithm with a time step of 1.0 fs was used to integrate the equations of motion. A cutoff distance of 20 Å was applied to all non-bonded interactions. All reported results were averaged over a 1000 ps simulation, with atomic coordinates and charges collected every 1.0 ps for post-analysis.

2026 S.-T. Yau High School Science Award
仅用于2026丘成桐中学科学奖论文公示

## 3. Results and Discussion

### Synthesis and Characterization of NiFe-LDH

FeNi-LDH array was fabricated on nickel foam (FeNi LDH/NF) by a simple solvothermal method by using $Fe(NO_3)_3 \cdot 9H_2O$ and $Ni(NO_3)_2 \cdot 6H_2O$ as metallic precursors, urea as the reductant (Figure 2a). The crystal structure of FeNi-LDH/NF was characterized by the X-ray diffraction (XRD) pattern (Figure 2b). Noting that the strong diffraction signals of nickel foam were removed to avoid the interference. The XRD pattern shows the characteristic reflections of NiFe-LDH. The strong peaks assigned to the (003) and (006) planes appear at approximately 11° and 23°, respectively, and additional reflections such as (012), (015), (018), and (113) are also visible. These peaks agree with the standard NiFe-LDH pattern (PDF#40-0215), confirming the expected layered structure[35, 38]. The morphology of the FeNi-LDH/NF was also analyzed by scanning electron microscopy (Figure 2c). NiFe-LDH/NF exhibits a network of interwoven nanosheets, which are supported by a multidimensional porous nickel-foam substrate, with each nanosheet having a lateral size of less than 200 nm. This nanoscale architecture facilitates the complete exposure of catalytic active sites and enhances the interaction between electrode and electrolyte. Furthermore, energy dispersive X-ray spectroscopy (EDS) elemental mapping confirmed the uniform distribution of Ni, Fe, and O throughout the NiFe-LDH (Figure 2d).

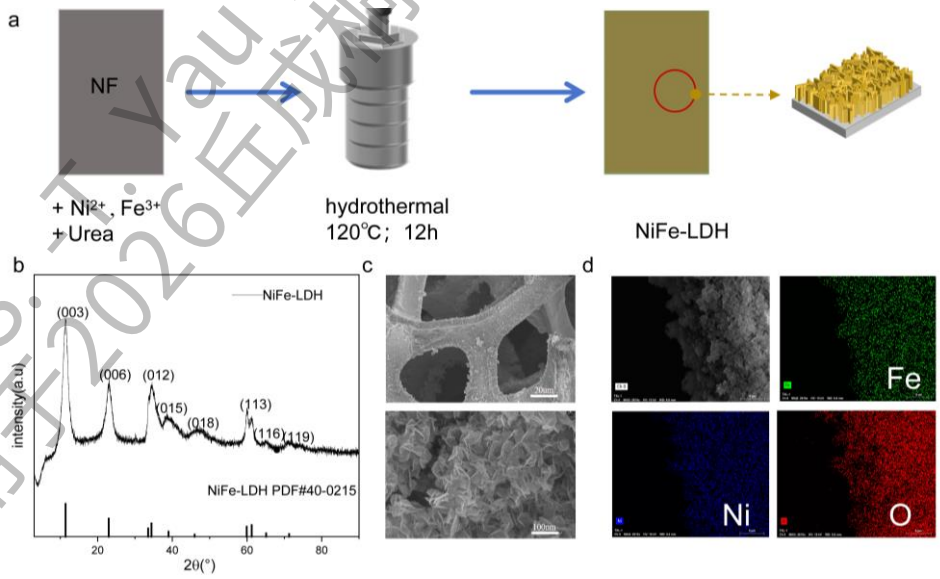



**Figure 2.** (a) Schematic route for the synthesis of NiFe-LDH. (b) XRD pattern, (c) SEM image, and (d) EDS elemental mapping of NiFe-LDH.

2026 S. T. Yau High School Science Award 仅用于2026丘成桐中学科学奖公示

**Electrocatalytic Performance and Durability of NiFe-LDH in Saline Environments**

To evaluate the individual and synergistic effects of $F^-$ and $B(OH)_4^-$ additives on the OER behavior of NiFe-LDH, cyclic voltammetry (CV) measurements were systematically performed in alkaline simulated seawater electrolytes containing different concentrations of coupled anion additives (Figure 3 and Figure 4). As shown in Figure 3, the introduction of F- alone gradually promoted OER activity, as evidenced by the decreased oxidation potential compared with the blank electrolyte, whereas $B(OH)_4^-$ alone exhibited a slight inhibitory effect, likely due to its interaction with the electrode/electrolyte interface. Subsequently, the synergistic effects of $F^-$ and $B(OH)_4^-$ were evaluated by varying their concentrations simultaneously (Figure 4).

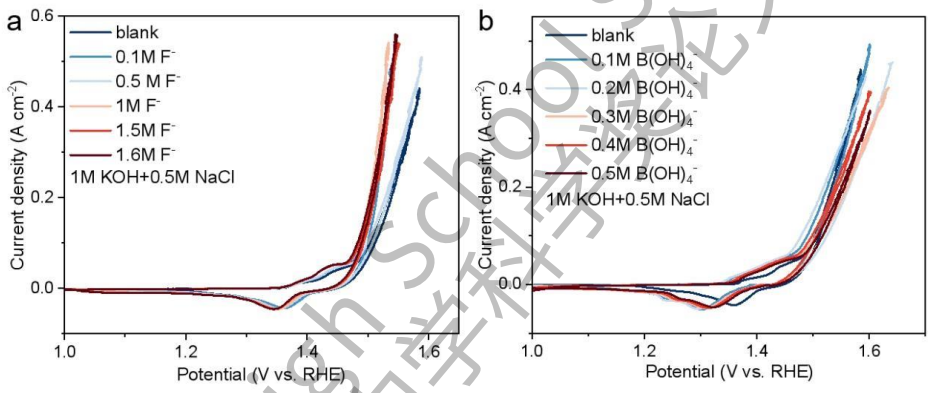



**Figure 3.** CV at alkaline simulated seawater containing (a) F- and (b) B(OH)4- additive, the scan rate is 5 mV/s.

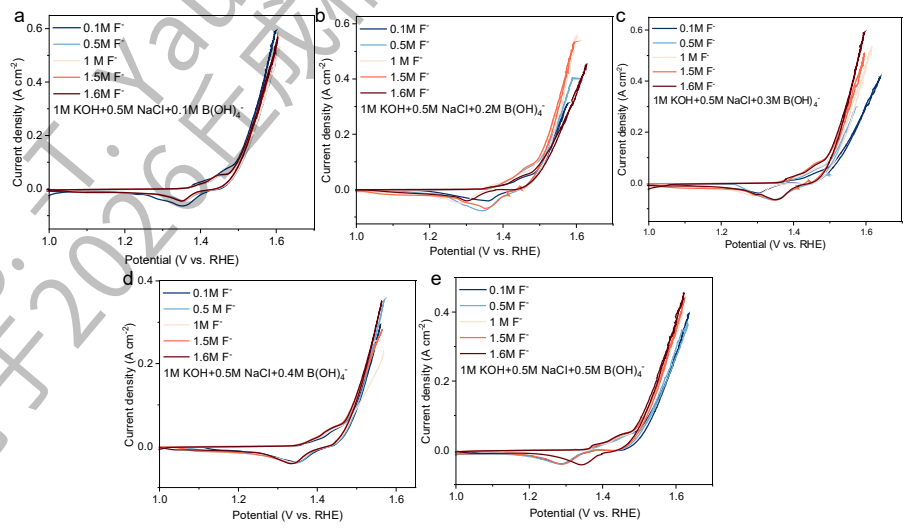



**Figure 4.** Cyclic voltammetry (CV) curves of NiFe-LDH in alkaline simulated seawater (1 M KOH + 0.5 M NaCl) containing different concentrations of $F^-$ and $B(OH)_4^-$ additives (scan rate: 5 mV $s^{-1}$):

2026 S.T.Yau High School Science Award
仅用于2026丘成桐中学科学奖公示

(a) 0.1 M $B(OH)_4^-$, (b) 0.2 M $B(OH)_4^-$, (c) 0.3 M $B(OH)_4^-$ (d) 0.4 M $B(OH)_4^-$ and (e) 0.5 M $B(OH)_4^-$ with $F^-$ concentrations of 0.1-1.6 M $F^-$ and (b) $B(OH)_4^-$

The overpotential values extracted at 10 mA $cm^{-2}$ from all CV curves were summarized into a two-dimensional activity map (Figure 5a). A low-overpotential region appears at relatively high (1.5–1.6 M) $F^-$ concentrations combined with moderate $B(OH)_4^-$ concentrations of about 0.1–0.4 M indicating an optimal electrochemical activity window for the $F^-$+$B(OH)_4^-$ synergistic electrolyte regulation. The effect of electrolyte composition on the stability of NiFe-LDH was further evaluated at 500 mA $cm^{-2}$ in a more corrosive and higher salty electrolyte containing 1 M KOH and 2 M NaCl (Figure 5b). Among these candidates, the electrolyte containing 1.5 M $F^-$ and 0.4 M $B(OH)_4^-$ helps NiFe-LDH to exhibit the most stable operation, identifying this composition as the optimized electrolyte for subsequent mechanistic investigations and device-level evaluation. For comparison, blank (1 M KOH + 0.5 M NaCl), $F^-$ (1 M KOH + 0.5 M NaCl + 1.5 M $F^-$), $B(OH)_4^-$ (1 M KOH + 0.5 M NaCl + 0.4 M $B(OH)_4^-$), $F^-$ + $B(OH)_4^-$ (1 M KOH + 0.5 M NaCl + 1.5 M $F^-$ + 0.4 M $B(OH)_4^-$) were investigated to distinguish the contributions of anions coupled effects. In Figure 5c, NiFe-LDH required an overpotential of approximately 234 mV to reach 10 mA $cm^{-2}$ in the blank electrolyte. The addition of $F^-$ significantly improved the OER activity, decreasing $\eta_{10}$ to approximately 223 mV, whereas $B(OH)_4^-$ alone showed a similar activity to the blank electrolyte with an $\eta_{10}$ of approximately 233 mV. When $F^-$ and $B(OH)_4^-$ were combined, a low $\eta_{10}$ of approximately 225 mV was maintained, demonstrating that the dual-anion electrolyte preserves favorable OER activity. All polarization curves were iR-corrected using the solution resistance determined by electrochemical impedance spectroscopy (EIS), excluding changes in solution resistance as the main origin of the observed activity differences. Corrosion polarization measurements further revealed the influence of the electrolyte additives on the corrosion behavior of NiFe-LDH (Figure 5d). The corrosion potential (Ecorr) progressively shifted from 0.867 V in the blank electrolyte to 0.909 V with $F^-$, 0.921 V with $B(OH)_4^-$, and 0.975 V in the $F^-$+$B(OH)_4^-$ electrolyte. The dual-anion system therefore exhibited the most positive corrosion potential, suggesting an improved corrosion-resistant interfacial environment. Together, these results indicate that $F^-$

2026 S. T. Yau High School Science Award
仅用于2026丘成桐中学科学奖论文公示

mainly contributes to the improvement in OER activity, while the combination of $F^-$ and $B(OH)_4^-$ provides a favorable balance between catalytic activity and corrosion resistance. This enhanced durability was further confirmed by chronopotentiometry at 1 A $cm^{-2}$ in 1 M KOH + 0.5 M NaCl (Figure 5e). The additive-free electrode failed after ~600 h due to a rapid potential increase, whereas the optimized $F^-$+$B(OH)_4^-$ electrolyte enabled stable operation for over 1500 h with only minor potential fluctuations. Thus, these results show that the optimized $F^-$+$B(OH)_4^-$ electrolyte significantly improves the corrosion resistance and high-current durability of NiFe-LDH.

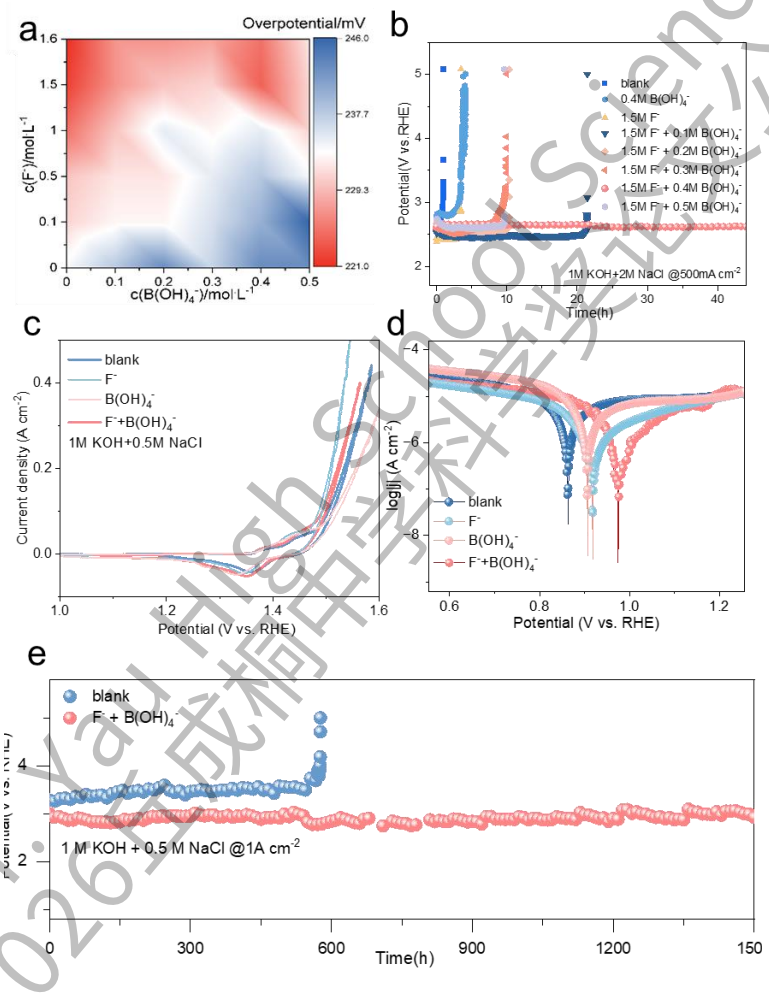



**Figure 5.** (a) Two-dimensional overpotential map at 10 mA $cm^{-2}$ as a function of $F^-$ and $B(OH)_4^-$ concentrations; the red region represents lower overpotential. (b) Chronopotentiometry (CP) tests at 500 mA $cm^{-2}$ in 1 M KOH + 2M NaCl at different $F^-$+$B(OH)_4^-$ compositions. (c) Polarization curves of NiFe-LDH with/without $F^-$+$B(OH)_4^-$ (d) corrosion polarization curves. (e) Chronopotentiometry (CP) tests at 1 A $cm^{-2}$ for NiFe-LDH in 1 M KOH + 0.5M NaCl.

Post-reaction SEM/EDS characterizations were carried out on NiFe-LDH

2026 S.-T. Yau High School Science Award
仅用于2026丘成桐中学科学奖公示

electrodes after 50 h chronopotentiometry tests at 1 A $cm^{-2}$ in alkaline seawater with different additives, which further verify the protective role of these anionic additives (Figure 6 and Table 1). The electrode tested in additive-free electrolyte exhibited severe structural degradation of both the catalyst layer and nickel foam substrate. In contrast, electrodes measured in $F^-$-, $B(OH)_4^-$-, and $F^-$+$B(OH)_4^-$-containing electrolytes retained the layered morphology of NiFe-LDH much better. Remarkably, the electrode cycled in the $F^-$+$B(OH)_4^-$ electrolyte maintained the most intact microstructure and possessed the lowest surface Cl content, demonstrating effective suppression of interfacial chloride accumulation and alleviation of chloride-triggered corrosion.

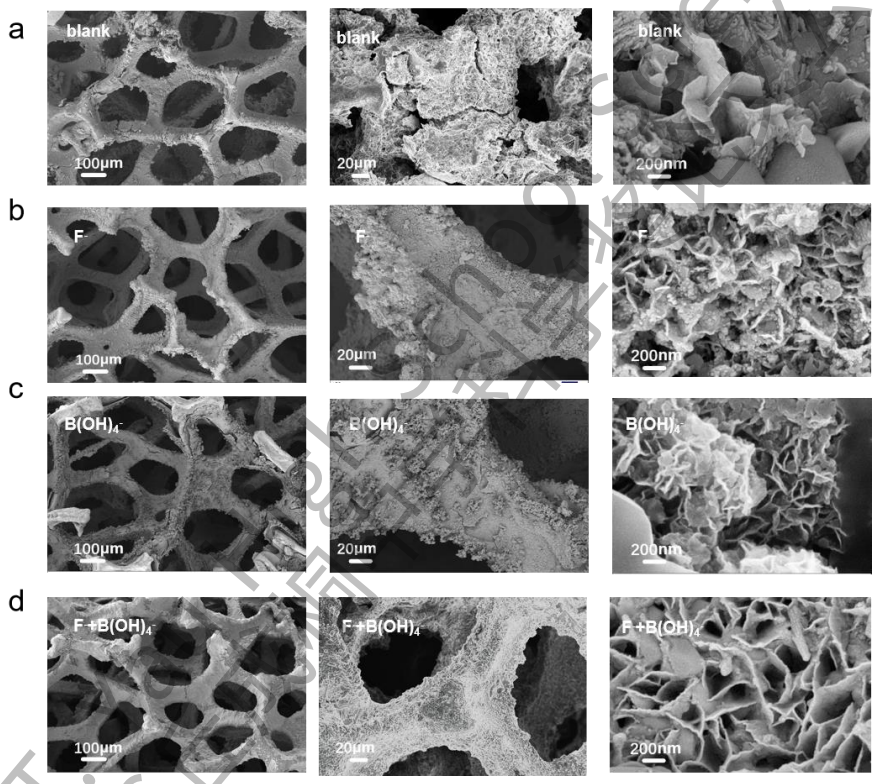



**Figure 6.** SEM images of NiFe-LDH electrodes after 50 h chronopotentiometry testing at 1 A $cm^{-2}$ in alkaline seawater with different additives.

**Table 1.** EDS analysis of Cl content on NiFe-LDH electrodes after 50 h chronopotentiometry (CP) at 1 A $cm^{-2}$ in alkaline seawater with different electrolytes.

| electrolyte | Wt% | At% | Apparent concentration |
|---|---|---|---|
| blank | 4.83 | 7.07 | 0.61 |
| $F^-$ | 1.75 | 1.52 | 0.27 |
| $B(OH)_4^-$ | 0.97 | 0.44 | 0.39 |
| $F^-$+$B(OH)_4^-$ | 0.16 | 0.1 | 0.04 |

2026 S.T. Yau High School Science Award
仅用于2026丘成桐中学科学奖公示

**Mechanism for Performance Enhancement of Dual-Ion System**

To investigate the origin mechanism of the enhanced seawater oxidation durability by the assistant with FB, we performed x-ray photoelectron spectroscopy (XPS) to probe the surface chemical environments of Ni and Fe before and after operation in different electrolytes. As shown in Figure 7a, following a 24-hours chronopotentiometric test at 400 mA $cm^{-2}$, the Fe 2p peak [38] of NiFe-LDH operated in the $F^-$, $B(OH)_4^-$, and $F^-$+$B(OH)_4^-$ electrolytes shifted toward higher binding energies by approximately 0.64, 0.34, and 0.28 eV, respectively, relative to that observed in the blank electrolyte (Figure 7a). The intermediate Fe shift observed in the co-additive electrolyte suggests that $F^-$ and $B(OH)_4^-$ jointly modulate the local coordination environment of Fe through their surface interactions. In contrast, only negligible changes (≤0.04 eV) were observed for the Ni 2p peaks under all additive-containing conditions (Figure 7b) [39]. These results indicate that the electrolyte additives predominantly tune the surface chemical environment of Fe, while the local chemical environment of Ni undergoes only minor variations. Meanwhile, F related signal clearly appeared after operation in the FB-containing electrolyte, further confirming the interaction between Fe with $F^-$ and $B(OH)_4^-$ (Figure 7c).

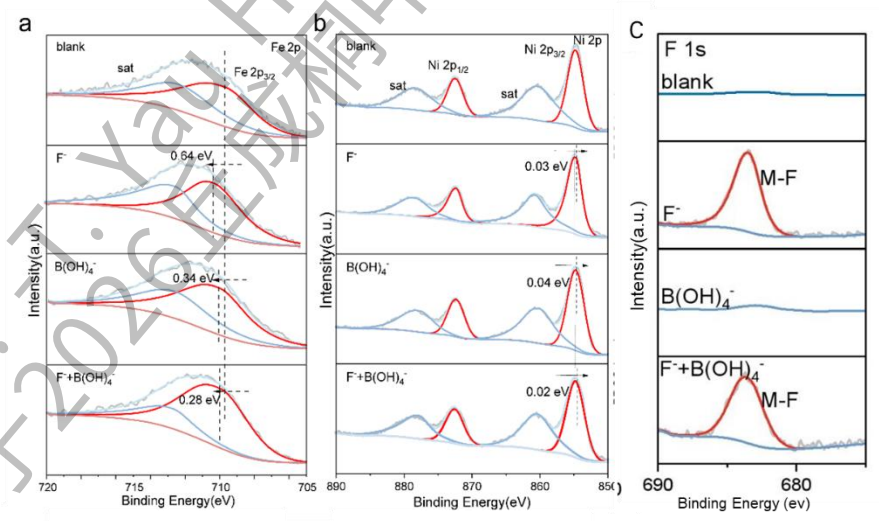



**Figure 7.** Electronic-state regulation of Ni/Fe dissolution by the $F^-$+$B(OH)_4^-$ electrolyte. (a) Fe 2p, (b) Ni 2p and (c) F 1s XPS spectra of NiFe-LDH after electrolysis in the blank, $F^-$, $B(OH)_4^-$, and $F^-$+$B(OH)_4^-$ containing electrolytes.

2026 S. T. Yau High School Science Award 仅用于2026年成都中学科学奖公示

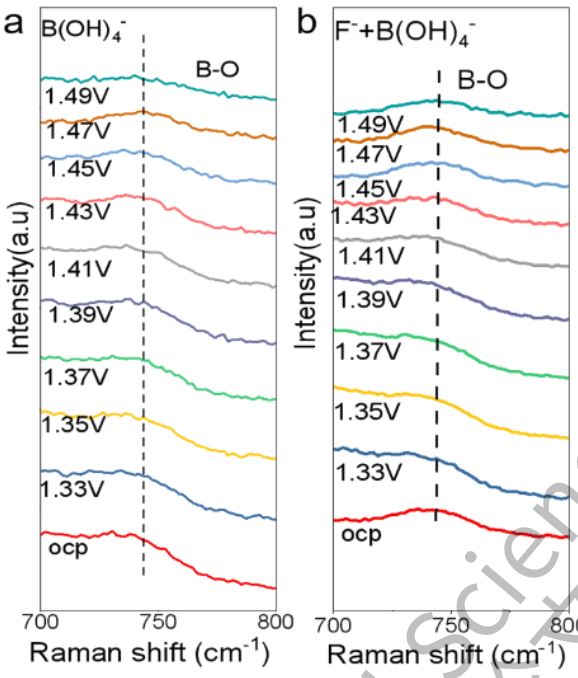



Figure 8. Operando Raman spectrum, in situ Raman spectra of the alkaline OER process at in simulated seawater and simulated seawater containing different additives. (a) $B(OH)_4^-$, (b) $F^-$ + $B(OH)_4^-$.

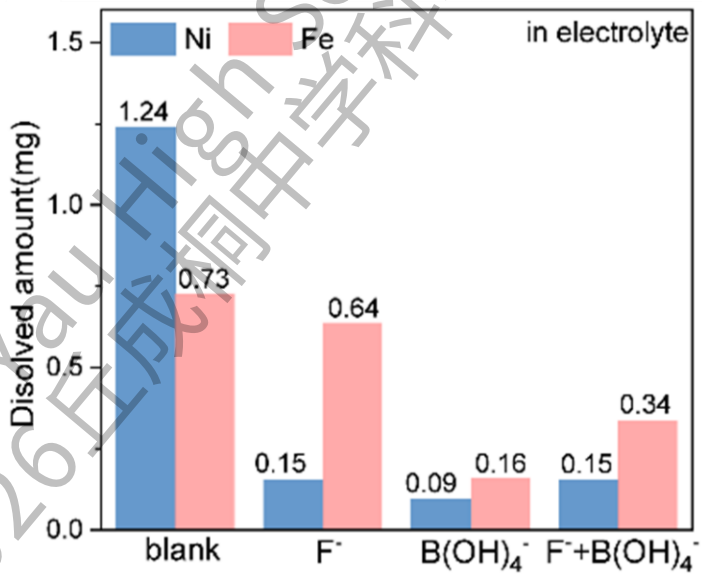



Figure 9. The dissolved amount of Ni and Fe after the 24 h chronopotentiometry (CP) test in different electrolytes

Furthermore, operando Raman spectroscopy observes borate-related B–O vibration, suggests the presence of borate species at the catalyst/electrolyte interface (Figure 8). The influence of electrolyte composition on the dissolution of metal during seawater oxidation was evaluated by inductively coupled plasma optical emission

2026 S. -T. Yau High School Science Award
仅用于2026丘成桐中学科学奖公示

spectroscopy (ICP-OES). As shown in Figure 9, the dissolved Ni amount from the NiFe LDH/NF in FB-containing electrolyte is 0.15 mg, which is significantly lower than that in the FB-free seawater (1.24 mg). Similarly, the dissolved Fe amount in FB-containing seawater is also lower than in FB-free electrolyte (Figure 9). These results demonstrated that their combination suppresses transition-metal dissolution, which provides sustained stabilization during prolonged electrolysis.

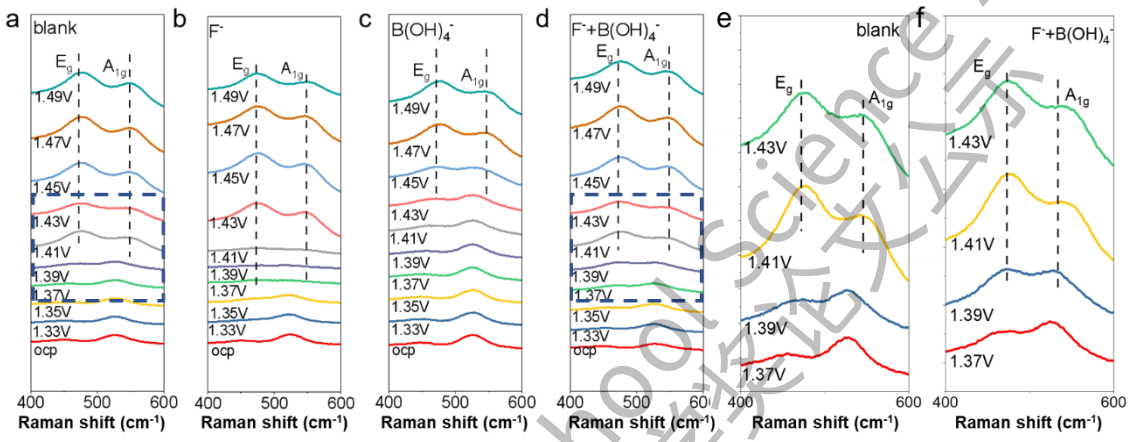



Figure 10. Operando Raman spectrum, in situ Raman spectra of the alkaline OER process at in simulated seawater and simulated seawater containing different additives. (a) blank, (b) F-, (c) B(OH)4-, (d) F- + B(OH)4-, e. enlarged view of the boxed region in a, f. enlarged view of the boxed region in d,

Operando Raman spectroscopy was further employed to track the potential-dependent reconstruction of NiFe-LDH (Figure 10). It showed the operando Raman spectra of NiFe-LDH in blank, $F^-$, $B(OH)_4^-$, and $F^-$+$B(OH)_4^-$ electrolytes over the potential range from open-circuit potential (OCP) to 1.49 V versus RHE. The NiFe-LDH in $F^-$+$B(OH)_4^-$ exhibited a shift of the peaks from 448 and 522 $cm^{-1}$ (corresponding to $Ni^{2+}$ Ni-O bending and stretching vibrations) to 469 and 547 $cm^{-1}$ ($Ni^{3+}$ Ni-O bending and stretching vibrations) at 1.39 V versus RHE. In contrast, NiFe-LDH in blank show surface reconstruction until at 1.41 V versus RHE. The earlier emergence of $Ni^{3+}$-O vibrations indicated that $F^-$+$B(OH)_4^-$ accelerates the initial reconstruction of NiFe-LDH into the catalytically active oxyhydroxide phase and enhances OER activity. Combined with XPS analysis after prolonged anodic polarization, these results revealed a dynamic regulation mechanism in which the electrolyte facilitates active-phase generation without producing a pronounced

2026 S. T. Yau High School Science Award
仅用于2026丘成桐中学科学奖公示

difference in the final Ni 2p binding energy after extended OER operation.

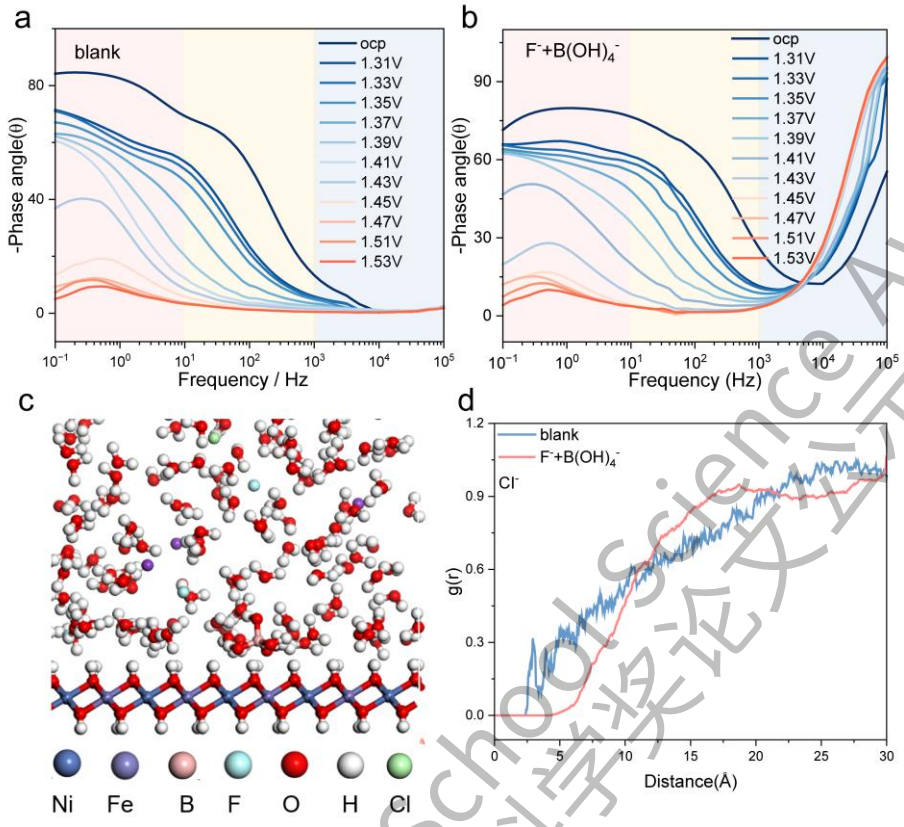



**Figure 11.** In situ EIS of NiFe-LDH in the ASSE (a) in blank and (b) $F^-+B(OH)_4^-$ electrolytes. (c) Representative molecular-dynamics snapshot of the NiFe-LDH/electrolyte. (d) The radial distribution of $Cl^-$ in different systems.

Operando Bode analysis was further employed to examine the interfacial electrochemical behavior of NiFe-LDH in both the FB-free (**Figure 11a**) and FB-containing electrolytes (**Figure 11b**). As the applied potential increased, the phase angle in the low- and intermediate-frequency regions gradually decreased in both systems. Notably, in comparison to the FB-free electrolyte, the phase angle in the FB-containing electrolyte decreased more rapidly, indicating enhanced interfacial electrochemical processes and more favorable OER kinetics. Furthermore, a significant difference was observed in the high-frequency region, where FB-containing electrolyte displayed a considerably larger phase angle above approximately $10^4$ Hz, suggesting an enhanced capacitive response at the catalyst-electrolyte interface. These results demonstrate that the dual-anion electrolyte not only accelerates the interfacial processes related to OER but also modifies the interfacial electrochemical behavior of NiFe-LDH.

2026 S. T. Yau High School Science Award
仅用于2026年成利中学科学奖论文公示

MD simulations provide a more direct molecular picture (Figure 11c). The representative configuration in Figure 9 contains the NiFe-LDH surface, water, $F^-$, $B(OH)_4^-$, and $Cl^-$. The differentiated distributions of $F^-$ and $B(OH)_4^-$ markedly alter the interfacial distribution of $Cl^-$. As shown by the $Cl^-$ radial distribution functions in 0.5M NaCl (Figure 9d), chloride begins to appear at approximately 2.0 Å from the NiFe-LDH surface in the blank electrolytes, whereas this onset shifts outward to about 5 Å in the $F^-$+$B(OH)_4^-$ electrolytes. This pronounced reduction confirms that the dual-anion electrolyte effectively suppresses chloride access to the catalyst surface.

Based on these results, a possible cooperative protection mechanism is proposed. $B(OH)_4^-$ contains multiple hydroxyl groups and can interact with the hydroxyl-rich NiFe-LDH surface and surrounding water molecules, while $F^-$ has strong hydration ability and interacts strongly with water. The coexistence of these two anions may therefore regulate the interfacial environment. Such an interfacial structure could reduce the approach and accumulation of $Cl^-$, thereby protecting NiFe-LDH from chloride-induced corrosion and metal dissolution during OER. Overall, the $F^-$+$B(OH)_4^-$ electrolyte provides a simple strategy to improve catalyst stability by regulating the local electrolyte environment rather than modifying the catalyst itself.

## 4. Conclusions

In this work, a simple dual-anion electrolyte strategy was developed to improve the durability of NiFe-LDH for alkaline saline-water oxidation. Systematic optimization identified 1.5 M $F^-$ + 0.4 M $B(OH)_4^-$ as the optimal electrolyte composition, decreasing the overpotential at 10 mA $cm^{-2}$ from approximately 234 mV in the blank electrolyte to 225 mV and enabling stable operation at 1 A $cm^{-2}$ for over 1500 h, compared with failure of the blank system after approximately 600 h. XPS and operando Raman spectroscopy supported the presence and interaction of $F^-$ and borate species at the catalyst/electrolyte interface, while ICP-OES measurements showed substantially reduced Ni and Fe dissolution, confirming enhanced resistance to catalyst degradation. Operando Bode analysis further revealed faster OER-related interfacial processes together with a pronounced high-frequency capacitive response in the dual-anion electrolyte. Combined with MD simulations showing that the closest distribution of $Cl^-$ was shifted away from the NiFe-LDH surface, these results suggest that $F^-$ and

2026 S.-T. Yau High School Science Award
仅用于2026丘成桐中学科学奖论文公示

$B(OH)_4^-$ cooperatively regulate the local interfacial environment. The hydroxyl-rich $B(OH)_4^-$ and strongly hydrated $F^-$ may regulate the interfacial environment and restrict $Cl^-$ accumulation near the catalyst, thereby suppressing corrosion and metal dissolution. This work demonstrates that rational electrolyte engineering provides a simple and effective approach to simultaneously enhance OER activity and long-term stability without requiring complicated modification of the catalyst itself, offering a promising strategy for durable alkaline saline-water electrolysis.

2026 S.-T. Yau High School Science Award
仅用于2026丘成桐中学科学奖论文公示

## 5. References


1 Sha Q, Wang S, Yan L, et al. 10,000-h-stable intermittent alkaline seawater electrolysis. *Nat*, 2025, 639(8054): 360-367

2 Zhou D, Li P, Lin X, et al. Layered double hydroxide-based electrocatalysts for the oxygen evolution reaction: Identification and tailoring of active sites, and superaerophobic nanoarray electrode assembly. *Chem Soc Rev*, 2021, 50(15): 8790-8817

3 Liu D, Cai Y, Wang X, et al. Innovations in electrocatalysts, hybrid anodic oxidation, and electrolyzers for enhanced direct seawater electrolysis. *Energy Environ Sci*, 2024, 17(19): 6897-6942

4 Wappler M, Unguder D, Lu X, et al. Building the green hydrogen market - current state and outlook on green hydrogen demand and electrolyzer manufacturing. *Int J Hydrogen Energy*, 2022, 47(79): 33551-33570

5 Huang J, Hu B, Meng J, et al. Highly efficient sustainable strategies toward carbon-neutral energy production. *Energy Environ Sci*, 2024, 17(3): 1007-1045

6 Tong W, Forster M, Dionigi F, et al. Electrolysis of low-grade and saline surface water. *Nat Energy*, 2020, 5(5): 367-377

7 Zhao C, Wang S. Harnessing dynamic reconstruction for intermittent seawater electrolysis. *Joule*, 2025, 9(6): 101969

8 Wu L, Xu Y, Wang Q, et al. Direct seawater electrolysis for green hydrogen production: Electrode designs, cell configurations, and system integrations. *Energy Environ Sci*, 2025, 18(10): 4596-4624

9 Dionigi F, Reier T, Pawolek Z, et al. Design criteria, operating conditions, and nickel–iron hydroxide catalyst materials for selective seawater electrolysis. *ChemSusChem*, 2016, 9(9): 962-972

10 Wu Z-J, Li J-H, Ying J, et al. Chloride ions resistance strategies in seawater electrolysis. *Small*, 2025, 21(31): 2504302

11 Feng S, Yu Y, Wang C, et al. Advances in durable electrocatalyst for seawater electrolysis applications. *Chem Catalysis*, 2025, 5(11): 101551

12 Feng C, Chen M, Yang Z, et al. Electrocatalytic seawater splitting for hydrogen production: Recent progress and future prospects. *J Met Sci Technol*, 2023, 162(203-226)

13 Song J, Zhang X, Pu G, et al. Towards chlorine-tolerant seawater electrolysis: Anode electrocatalysts, electrolyte, and system design strategies. *Sci China Mater*, 2025, 69(1): 28-43

14 Trotochaud L, Young SL, Ranney JK, et al. Nickel–iron oxyhydroxide oxygen-evolution electrocatalysts: The role of intentional and incidental iron incorporation. *J Am Chem Soc*, 2014, 136(18): 6744-6753

15 Dresp Sr, Dionigi F, Klingenhof M, et al. Direct electrolytic splitting of seawater: Opportunities and challenges. *ACS Energy Lett*, 2019, 4(4): 933-942


2026 S.-T. Yau High School Science Award 仅用于2026年成师中学科学奖论文公示

16 Kuang Y, Kenney MJ, Meng Y, et al. Solar-driven, highly sustained splitting of seawater into hydrogen and oxygen fuels. *Proc Natl Acad Sci*, 2019, 116(14): 6624-6629
17 Su X, Wang Y, Zhou J, et al. Operando spectroscopic identification of active sites in nife prussian blue analogues as electrocatalysts: Activation of oxygen atoms for oxygen evolution reaction. *J Am Chem Soc*, 2018, 140(36): 11286-11292
18 Yu F, Kang X, Liu J, et al. A current-adaptive polyoxovanadates protected anode for efficient and stable ampere-level seawater electrolysis. *Adv Mater*, 2026, 38: e74085
19 Zhang Y, Xu Y, Zhou Q, et al. Achievements, challenges and opportunities in hydrogen production from water/seawater splitting using boron-based materials. *Sci China Mater*, 2025, 68(2): 341-363
20 Wang Z, Niu X, Ye L, et al. Boron modification promoting electrochemical surface reconstruction of nife-ldh for efficient and stable freshwater/seawater oxidation catalysis. *J Colloid Interface Sci*, 2024, 668(607-617)
21 Chen L, Ma F, Yin S, et al. Nife-layered double hydroxides nanosheets coordinated with terephthalic acid: Preferentially adsorbing $OH^-$ but repelling $Cl^-$ during alkaline seawater oxidation. *ACS Sustainable Chem Eng*, 2026, 14(14): 6812-6822
22 Chen L, Ma F, An Y, et al. Self-supporting FeOOH/NiFe-LDH heterostructures with a built-in electric field for efficient and durable alkaline seawater oxidation. *J. Phys. Chem. Let*, 2026, 17(7): 2118-2127
23 Liu Y, Guo J, Liu X, et al. Corrosion-driven $Ni_3S_4$ gradient in NiFe-LDH enables durable industrial-scale water electrolysis. *Angew Chem Int Ed*, 2025, 64(49): e202516894
24 Yang L, Xing Z, Chen Y, et al. Anion shielding in Nb-$WO_3$/$WS_2$ heterostructures: A strategy for efficient and corrosion-resistant seawater electrolysis. *Small*, 2025, 21(51): e09761
25 Liu W, Yu J, Sendeku MG, et al. Ferricyanide armed anodes enable stable water oxidation in saturated saline water at 2 A/$cm^2$. *Angew Chem Int Ed*, 2023, 62(40): e202309882
26 Liu W, Yu J, Li T, et al. Self-protecting cofeal-layered double hydroxides enable stable and efficient brine oxidation at 2 A/$cm^2$. *Nat Commun*, 2024, 15(1): 4712
27 Ma T, Xu W, Li B, et al. The critical role of additive sulfate for stable alkaline seawater oxidation on nickel-based electrodes. *Angew Chem Int Ed*, 2021, 60(42): 22740-22744
28 Yu M, Li J, Liu F, et al. Anionic formulation of electrolyte additive towards stable electrocatalytic oxygen evolution in seawater splitting. *J Energy Chem*, 2022, 72(361-369)
29 He X, Yao Y, Zhang L, et al. Hexafluorophosphate additive enables durable seawater oxidation at ampere-level current density. *Nat Commun*, 2025, 16(1): 4998

2026 S.T. Yau High School Science Award
仅用于2026丘成桐中学科学奖公示

30 Ye L, Ding Y, Niu X, et al. Unraveling the crucial contribution of additive chromate to efficient and stable alkaline seawater oxidation on ni-based layered double hydroxides. *J Colloid Interface Sci*, 2024, 665(240-251)
31 Yu Y, Zhou W, Yuan J, et al. A hydrogen-bond network sieve enables selective $OH^-$ /$Cl^-$ discrimination for stable seawater splitting at 2.0 A/$cm^2$. *Energy Environ Sci*, 2025, 18(22): 9949-9958
32 Che Y, Shang J, Zhang Y, et al. In situ engineering a dual-anion rejection interface for high-efficiency oxygen evolution in alkaline seawater. *Adv Funct Mater*, 2025, 35(43): 2507544
33 Liu T, Chen Y, Hao Y, et al. Hierarchical anions at the electrode-electrolyte interface for synergized neutral water oxidation. *Chem*, 2022, 8(10): 2700-2714
34 Cheng J, Liu W, Chen S, et al. Fluoride-engineered electrolyte for highly stable and efficient alkaline seawater electrolysis at 2 A/$cm^2$. *Angew Chem Int Ed*, 2025, 64(52): e18106
35 Komiya H, Obata K, Wada M, et al. Electrolyte engineering applying concentrated chloride ions with mixed buffer solutions for a versatile high-productivity water-splitting system. *ACS Sustainable Chem Eng*, 2023, 11(34): 12614-12622
36 Qi W, Zeng Y, Wang L, et al. Stabilizing amorphous nife-based catalysts via borate bridging for water oxidation under industrial conditions. *EES Catalysis*, 2025, 3(6): 1369-1376
37 Li T, Yang C, Cai Z, et al. Surface borate layer dramatically enhances the stability of NiFe-layered double hydroxide for alkaline seawater oxidation. *Materials Today Physics*, 2025, 50(101612
38 Li P, Duan X, Kuang Y, et al. Tuning electronic structure of NiFe layered double hydroxides with vanadium doping toward high efficient electrocatalytic water oxidation. *Adv Energy Mater*, 2018, 8(15): 1703341
39 Shi Y, Song L, Liu Y, et al. Dual cocatalytic sites synergize NiFe layered double hydroxide to boost oxygen evolution reaction in anion exchange membrane water electrolyzer. *Adv Energy Mater*, 2024, 14(46): 2402046

2026 S. -T. Yau High School Science Award
仅用于2026丘成桐中学科学奖论文公开

## 6. Acknowledgements

Thanks for the opportunity offered by Prof. Sun to enter the university's lab and learn to do experiments.

Thanks for lecturing us about the concepts in this field.

Thanks to the master’s student, Tian Xinling, in Prof. Sun's group for all the instruction and advice when I did the experiment and when I wrote this research article.

Thanks to my teacher, Zhu Lin for her guidance in experiments and paper writing. Thanks for all the support that I have received so far.

Note that the topic was confirmed after I found and studied the field I was interested in and discussed it with Prof. Sun Xiaoming.

I did not use any AI tools during the entire experiment and paper preparation.

Most of the experiment was done on my own and the data were collected on my own. The analysis of the data was partially helped by Tian Xinling. The paper was completed on my own.

2026 S. -T. Yau High School Science Award
仅用于2026丘成桐中学科学奖论文公示